CSigma graphs: a new approach for plasma characterization in laser-induced breakdown spectroscopy

C. Aragón* and J.A. Aguilera

Departamento de Física, Universidad Pública de Navarra, Campus de Arrosadía,
E-31006 Pamplona, Spain

Abstract

A generalization of curves of growth called CSigma ($C\sigma$) graphs, which allows including several lines of various elements in the same ionization state at different concentrations, is proposed for laser-induced breakdown spectroscopy (LIBS) experiments. The method relies on the Boltzmann, Saha and radiative transfer equations for plasmas in local thermodynamic equilibrium. $C\sigma$ graphs are based on the calculation of a line cross section σ_l for each of the experimental data, starting from the atomic data of the line, the temperature and the electron density. A model of homogeneous plasma, applied separately for neutral atoms and ions, is used. A limit of validity is established for this model. Experimental $C\sigma$ graphs have been obtained using fused glass samples containing Fe, Mn, Mg, Si and Cr. By fitting experimental $C\sigma$ graphs to calculated curves, the LIBS system becomes characterized by a set of four parameters βA, Nl, T, N_e, different for neutral atoms and ions. Starting from this characterization, the intensity and self-absorption of a given spectral line of an element at a certain concentration may be predicted, provided that its atomic data are known and the limit of validity is not exceeded.

Keywords:
Laser-induced breakdown spectroscopy; LIBS; Plasma characterization; Curves of growth; CSigma graph

*Corresponding author.
Phone: +34 948169579
Fax: +34-948169565.
E-mail address: carlos.aragon@unavarra.es

1. Introduction

Since the advent of laser-induced breakdown spectroscopy (LIBS), the characterization of laser-induced plasmas has been a useful tool for improving the knowledge and applications of these sources of radiation. The main characteristic parameters of the plasma, i.e., the electron temperature and density, may be determined by optical emission spectroscopy using methods as the Boltzmann or Saha-Boltamann plots for temperature measurement and the Stark broadening of line profiles to determine the electron density [1,2]. One of the requirements for accurate characterization by these methods is the use of optically thin spectral lines. In the early works on LIBS including plasma characterization, optically thin conditions were verified by checking the experimental ratio of line intensities. Radziemski et al. [3] measured the time-resolved temperatures and electron densities of laser-induced plasmas generated in aerosols in air. It was verified that the plasma was optically thin from the intensity ratio of a N I triplet. Simeonsson and Miziolek [4] studied laser-produced plasmas in CO, CO_2, methanol and chloroform and checked the ratio of emission intensities of three O I lines. Sabsabi and Cielo [5] characterized laser-induced plasmas generated from aluminium alloys containing 0.7 % Fe, determining the excitation temperature from the Fe I emission by the Boltzmann plot method and the electron density from the Stark broadening of Al II lines. To verify that the Fe I lines were optically thin, they used the ratio of resonant and nonresonant lines, whereas in the case of the Al II lines, they estimated the absorption coefficients.

Several works have proposed procedures for correcting self-absorption as a preliminary step towards characterization of laser-induced plasmas by the mentioned optical emission spectroscopy techniques [6-10]. Among these works, we may distinguish that of Moon et al. [10], where the method based on the use of a duplicating mirror is illustrated, proving its usefulness in evaluating the effect of self-absorption. It is shown that this method allows improving the accuracy in temperature determination from Saha-Boltzmann plots as well as the linearity of analytical calibration curves.

A different approach for plasma characterization consists in using methods which take into account intrinsically the self-absorption of spectral lines. For example, Hermann et al. [11], performed the diagnostics of the early phase of a laser-induced plasma generated from a Ti target in low pressure N_2 atmosphere considering self-absorption. By comparing computed line profiles with the experimental ones, the temperature, electron density and densities of emitting species were determined. A similar approach was used by D'Angelo et al. [12,13] for a laser-induced plasma generated from a ternary alloy Co-Cr-Mo. In [12], a two-region plasma picture of a hot dense core surrounded by a colder periphery was considered whereas a cilynder-symmetrical plasma column with a parabolic temperature distribution was used in [13]. A heuristic model for LIBS was developed by Wester and Noll [14], based on the use of the radiation transport equation to calculate the spectrum emitted by the laser-induced plasma, described by a two-shell model surrounded by ambient gas. Simulations of a multiline iron spectrum and a self-reversed Al line were compared with experimental spectra. Gornushkin et al. [15] developed a simplified approach for modelling an inhomogeneous optically thick laser induced plasma. The model predicts spatial and temporal distributions of atom, ion and electron number densities, evolution of an atomic line profile and optical thickness and the resulting absolute intensity of plasma emission in the vicinity of a strong non-resonance atomic transition. The same group reported a method of temperature measurement based on an optically thick inhomogeneous laser-induced plasma [16]. The method provides maximum temperature in the plasma center from the intensity ratio of two self-reversed lines. Cristoforetti and Tognoni [17] have recently proposed the calculation of the elemental columnar density (i.e. the total atomic number density times the length of the plasma along the line-of-sight) from self-absorbed lines as a useful tool for analysing the composition of laser-induced plasmas and for their characterization.

Another approach for investigating laser-induced plasmas in optically thick conditions is the use of curves of growth (COGs). The first application of the COG concept to LIBS was carried out by Gornushkin et al. [18]. In this work, theoretical and experimental COGs were obtained for a resonance chromium line in laser-induced plasmas generated from steel samples. The damping constant and the density of neutral chromium atoms were deduced from the best fit of the calculated COG to the experimental points. Lazic et al. [19] developed a simplified self-absorption model and applied it to generate the calibration curves, which are in fact COGs, for LIBS measurements on soils and sediments. Our group has also reported works on the COG methodology applied to LIBS. In [20], the COGs of seven Fe I lines emitted from laser-induced plasmas generated from Fe-Ni alloys were measured, finding good correlation between experimental and calculated results. The results of this study were extended in [21] to lines belonging to different multiplets, having different level energies and line widths, with the aim of studying the influence of the temporal evolution and spatial inhomogeneity of the plasma. In [22], the COGs of ionic Fe II lines were studied in addition to neutral Fe I lines. It was shown that a reduced set of plasma parameters resulting from the COGs, may be used to characterize the plasma. These parameters include the temperature, the electron density and the columnar density of the emitting species for 100% concentration. The temporal evolution of the characteristic plasma parameters deduced from the COGs, and their usefulness for obtaining the intensity of self-absorbed lines were investigated in a later work [23].

In all the previous works dealing with the application of COGs to LIBS, the optical depth has been varied using several samples with different elemental concentrations in order to change the number density of

the emitting species in the plasma. Indeed, in all cases the COGs are defined as graphs of the intensity of a given line versus the concentration of the emitting element in the sample. However, apart from the number density and the optical path varied in the duplicating mirror experiments [10], the optical depth depends also on other quantities, which may be divided into, on one side, a group including the oscillator strength, the partition function and the Boltzmann factor corrected for stimulated emission and, on the other side, the line shape. The effect of the first group of parameters is quantified in the k_t coefficient, introduced in our previous work [20], which depends on the oscillator strength and other atomic data of the transition as well as on the plasma temperature. The k_t concept has been used by other groups to estimate self-absorption in LIBS experiments [24-28] or as a starting point for the development of self-absorption models [9,12,13]. However, the k_t coefficient allows comparing the optical depth of lines of a given element and ionization state if the lines have the same line shape. The objective of the present work is the generalization of COGs to a graph which allows including several lines emitted by different elements in the same ionization state present in one or more concentrations. Also we aim at improving the concept of the k_t coefficient, looking for a parameter useful to compare the optical depth of spectral lines of different widths and emitted by elements having different ionization ratios in the plasma.

2. Method

2.1 Basic equations and k_t coefficient

The equations used in the method developed in this work are those of the theory of plasmas in local thermodynamic equilibrium (LTE) [29]. The local electron temperature T describes in each position the population of the energy levels of the atoms or ions of the plasma by means of the Boltzmann equation. From the population, the wavelength-integrated emission coefficient (W m^{-3} sr^{-1}) for a spectral line emitted by an atom of an element α in an ionization state z is deduced as a function of the atomic data of the transition and of the numerical density of emitters N_α^z (m^{-3})

$$\varepsilon = \frac{hc}{4\pi\lambda_0} A_{ki} \frac{N_\alpha^z}{U_\alpha^z(T)} g_k e^{-\frac{E_k}{kT}}, \tag{1}$$

where h (J s) is the Planck constant, c (m s^{-1}) is the speed of light in vacuum, k (eV K^{-1}) is the Boltzmann constant, A_{ki} (s^{-1}) is the transition probability, g_k (dimensionless) and E_k (eV) are the degeneration and the energy of the upper level of the transition, λ_0 (Å) is the central wavelength of the transition and $U_\alpha^z(T)$ (dimensionless) is the partition function of the emitting species. The representation of $\ln\left[\varepsilon\lambda_0/(A_{ki}g_k)\right]$ as a function of E_k, called a Boltzmann diagram, leads to a straight line with a negative slope $-1/(kT)$, from which the temperature can be obtained.

Furthermore, in LTE, the local temperature value and electron density N_e (m^{-3}) value determine by means of Saha equation the relationship between the numerical densities of species in consecutive ionization states. Using $z = 0$ for neutral atoms and $z = 1$ for singly-ionized atoms, the Saha equation provides the ratio

$$S^{10}(T, N_e) = \frac{N_\alpha^1}{N_\alpha^0} = \frac{2U_\alpha^1}{N_e U_\alpha^0}\left(\frac{mkT}{2\pi\hbar^2}\right)^{3/2} \exp\left(-\frac{E_\infty^0 - \Delta E_\infty^0}{kT}\right), \tag{2}$$

where $\hbar = h/2\pi$, m (kg) is the mass of the electron, E_∞^0 (eV) is the ionization energy and ΔE_∞^0 (eV) is the correction thereof due to interactions in the plasma.

Finally, the existence of LTE allows using the radiative transfer equation. Its integration, considering an homogeneous plasma having a length l (m) along the line of sight leads to the following expression for the wavelength-integrated line intensity measured in counts

$$I = \beta A L_P \int_{\text{line}} \left(1 - e^{-\tau(\lambda)}\right) d\lambda = \beta A L_P \int_{\text{line}} \left(1 - e^{-k'(\lambda)l}\right) d\lambda, \tag{3}$$

where A (m^2) is the transverse area of the region of the of the plasma whose emission is detected, β is the instrumental factor of the system (counts W^{-1} sr) equal to the product of the spectral efficiency times the solid angle of detection, and $L_P = L_P(\lambda_0, T)$ is the Planck radiance (Wm^{-2}sr^{-1}Å^{-1}) of a blackbody at temperature T and wavelength λ_0, which is considered constant in the integration over the line profile. The line intensity depends on the optical depth $\tau(\lambda)$ (dimensionless), which in the case of an homogeneous plasma is expressed

as $\tau(\lambda) = k'(\lambda) l$, where $k'(\lambda)$ is the effective absorption coefficient (m^{-1}). According to Eq. (3), a plot of the intensity as a function of the optical depth is known as curve of growth (COG). In a previous work [20], the coefficient $k_t(T)$ (m^2 Å) for a transition, dependent on the atomic data of the transition and the temperature, was defined by

$$k_t = \frac{e^2 \lambda_0^2}{4\varepsilon_0 mc^2} f \frac{g_i e^{-\frac{E_i}{kT}}}{U_\alpha^z(T)} \left(1 - e^{-\frac{E_k - E_i}{kT}}\right) = \frac{\lambda_0^4}{8\pi c} A_{ki} \frac{g_k e^{-\frac{E_i}{kT}}}{U_\alpha^z(T)} \left(1 - e^{-\frac{E_k - E_i}{kT}}\right), \quad (4)$$

where ε_0 (Fm^{-1}) is the permittivity of vacuum, g_i (dimensionless) and E_i (eV) the degeneration and the energy of the lower level and f (dimensionless) the oscillator strength. Using the k_t coefficient, the effective absorption coefficient may be factorized as follows

$$k'(\lambda) = k_t N_\alpha^z V(\lambda), \quad (5)$$

where $V(\lambda)$ (Å^{-1}) is the normalized line shape, which we assume to be a Voigt profile. The normalized Voigt profile depends on the Doppler width $\Delta\lambda_D$ (Å) and on the damping constant a (dimensionless), defined as

$$a = (\ln 2)^{1/2} \frac{\Delta\lambda_N + \Delta\lambda_L}{\Delta\lambda_D} \approx (\ln 2)^{1/2} \frac{\Delta\lambda_L}{\Delta\lambda_D}, \quad (6)$$

where $\Delta\lambda_N$ (Å) and $\Delta\lambda_L$ (Å) are the natural and Lorentzian widths, respectively. The Doppler width can be estimated starting from the temperature T by the expression [30]

$$\Delta\lambda_D = \left(\frac{8kT \ln 2}{Mc^2}\right)^{1/2} \lambda_0 \ , \quad (7)$$

where M (kg) is the mass of the emitting atom. Due to the high electron density in laser-induced plasmas, it can generally be assumed that the main broadening mechanism is the Stark effect. As a result, the Lorentzian width of a spectral line can be obtained from the electron density N_e if its Stark width is known. In turn, the electron density in the plasma can be determined from the measurement in the experimental spectrum of the Lorentzian width of a line the Stark width of which is known and large enough.

2.2 Ionization factor r_i

By assuming that the laser-induced plasma is only formed by neutral atoms and ions with a unit charge, the density of an element α in the plasma will be

$$N_\alpha = N_\alpha^0 + N_\alpha^1, \quad (8)$$

where N_α^0 and N_α^1 are the densities of neutral atoms and ions with a unit charge, respectively. From equations (2) and (8) it is deduced that the densities of neutral atoms and ions in the plasma can be expressed as

$$N_\alpha^z = r_i N_\alpha, \quad (9)$$

where $r_i(N_e, T)$ (dimensionless) is an ionization factor, defined as follows

$$r_i = \frac{1}{1 + S^{10}} \quad \text{for neutral atoms,} \quad (10a)$$

$$r_i = \frac{S^{10}}{1 + S^{10}} \quad \text{for ions of unit charge.} \quad (10b)$$

If we assume that the stoichiometry in the ablation process is maintained, such that it is the same in the plasma as in the sample, the following relationship is met

$$C = 10^2 \frac{N_\alpha}{N}, \tag{11}$$

where N is the total density in the plasma and C is the concentration of the element in the sample expressed in atomic percentage (at. %). By substituting equations (9) and (11) into equation (5), the optical depth may be expressed as

$$\tau(\lambda) = 10^{-2} C\ Nl\ k_t r_i\ V(\lambda), \tag{12}$$

where we see that the optical depth is proportional to several factors, including the concentration $10^{-2}C$, the columnar density Nl (m^{-2}), the k_t coefficient, the ionization ratio r_i and the line profile $V(\lambda)$. It is worth stressing that the density N in the columnar density is the total number density, including atoms and ions with a unit charge for all the elements.

2.3 Line cross section σ_l

In our quest to obtain a generalized COGs including several lines of different elements in the same ionization state, we have plotted in a graph the line intensity normalized to the Planck radiance I / L_P as a function of the quantity $10^{-2} C\ k_t r_i$. To obtain the intensity, the integral in equation (3) has been calculated numerically, using the polynomial approximations described in [30] to calculate the Voigt profile. Fig. 1 shows the resulting curves, obtained for a typical Doppler width $\Delta\lambda_D$ = 0.03Å and Lorentzian widths $\Delta\lambda_L$ in a range from 0.01 Å to 1 Å, corresponding to damping constants a from 28 to 0.28. All the curves have the same optically thin linear limit for $Ck_t r_i \to 0$, shown in the figure, whose slope has been arbitrarily chosen as $\beta ANl = 10^{20}$ counts $W^{-1}sr$. As can be seen, the curves for the various Lorentzian widths differ from each other even for small values of the abscissa. The interpretation of the graph in Fig. 1 is clear: the strong influence of the line shape in the absorption of a spectral line leads to very distinct curves, which makes this type of graph unsuitable for including lines of a given species having different Lorenztian widths.

By averaging over the line shape, a line effective absorption coefficient (m^{-1}) may be defined as follows

$$k_l = \frac{1}{\Delta\lambda_L} \int_{line} k'(\lambda)\, d\lambda = k_t r_i N_\alpha \frac{1}{\Delta\lambda_L}. \tag{13}$$

A similar definition is made of an adimensional line optical depth, which may be expressed as

$$\tau_l = k_l\ l = k_t r_i N_\alpha l \frac{1}{\Delta\lambda_L}. \tag{14}$$

As described in [30,32], absorption is sometimes expressed in terms of the absorption cross section $\sigma(\lambda)$ (m^2) defined as the absorption coefficient per absorbing atom or ion

$$\sigma(\lambda) = k(\lambda) / N_\alpha^z. \tag{15}$$

In the book by Zel'dovich and Raizer [32], the absorption cross section is interpreted as follows. Considering a parallel beam of light rays of wavelength λ and unit cross-sectional area travelling through an absorbing gas, if each atom or ion is replaced by an opaque disc of section $\sigma(\lambda)$ perpendicular to the direction of the beam, we can visualize absorption as a process of the capture of the photons which strike the discs. We now replace in equation (15) the absorption coefficient $k(\lambda)$ with the effective absorption coefficient $k'(\lambda)$, corrected for stimulated emission, so the absorption cross section becomes the effective absorption cross section $\sigma'(\lambda) = k'(\lambda) / N_\alpha^z$. Then, the number density N_α^z of atoms or ions is replaced with the total number density N_α for an element, so the new cross section becomes $\sigma^*(\lambda) = k'(\lambda) / N_\alpha = r_i \sigma'(\lambda)$. We then average over the line shape, defining a line cross section $\sigma_l(T, N_e)$ (m^2) as

$$\sigma_l = \frac{1}{\Delta\lambda_L} \int_{line} \sigma^*(\lambda)\, d\lambda = r_i \frac{1}{\Delta\lambda_L} \int_{line} \sigma'(\lambda)\, d\lambda. \tag{16}$$

The line cross section is related to the line effective absorption coefficient by the equation

$$\sigma_l = k_l / N_\alpha , \tag{17}$$

which is analogous to equation (15). Equation (17) allows making for the line cross section σ_l the same interpretation made by Zel'dovich and Raizer for $\sigma(\lambda)$ with two differences: N_α^z is replaced with N_α, so both atoms and ions of an element are considered, and the process includes stimulated emission together with absorption, as the coefficient *k*' is used instead of *k*. From equations (13) and (17) the line cross section may be expressed as

$$\sigma_l = k_t r_i \frac{1}{\Delta\lambda_L} . \tag{18}$$

As we will see in the next subsection, the line cross section is an important parameter for achieving the generalized COGs. It is made up of three factors that characterize three distinct dependences of the optical depth of a line: (1) the k_t coefficient, which is proportional to the line intensity in the optically thin limit normalized to the Planck radiance, of a transition of a given element in an ionization state; (2) the ionization factor r_i, which accounts for the different ionization degree of elements; and (3) the factor $1/\Delta\lambda_L$, accounting for the effect of the line profile. If we multiply σ_l by the remaining two factors affecting the optical depth, namely the density $N_\alpha = 10^{-2} CN$ and the length along the line-of-sight *l*, we get the line optical depth

$$\tau_l = 10^{-2} C\ Nl\ \sigma_l . \tag{19}$$

2.4 Cσ graphs

If we divide the abscissa in the graph of Fig. 1 by $\Delta\lambda_L$, we obtain $10^{-2} C\sigma_l$ and, dividing also the ordinate, we get the curves shown in Fig. 2. As can be seen, except for the case of a Lorentzian width in the order of 0.01 Å or lower, which is rather uncommon in laser-induced plasmas, the curves are very close. The plot in the inset shows that the curves become more similar as the abscissa decreases, and tend towards their linear limit as $C\sigma_l \to 0$. More strictly, the shape of the curves depends on the damping ratio *a*, and the practical coincidence of the curves takes place for *a* > 1 [33]. The similarity of the curves of Fig. 2 for lines having different Lorentzian widths suggests the construction of a graph from the experimental data with $I / \left(L_P \Delta\lambda_L\right)$ as the ordinate and $10^{-2} C\sigma_l$ as the abscissa, which we have called *Cσ* graph. From Fig. 2, we see that it is expected from theory that, when lines of different widths are included in the *Cσ* graph, the data will follow a quite smooth behaviour, with the mentioned common linear limit for low $C\sigma_l$ values. The *Cσ* graphs constitute the generalized COGs whose definition and experimental verification are the objectives of the present work. Theoretical values of the ordinate of *Cσ* graphs may be obtained by numerical calculation of the integral in equation (3), obtaining a calculated *Cσ* curve, which may be expressed as

$$\frac{I}{L_P \Delta\lambda_L} = f\left(10^{-2} C\sigma_l\right). \tag{20}$$

According to equations (3) and (12), the *Cσ* curve depends on four parameters, namely: *βA*, *Nl*, *T*, N_e. As will be seen in the next section, the parameters *βA*, *Nl* and *T* may be deduced from the fitting of the experimental *Cσ* graph to calculated *Cσ* curves. The linear relationship obtained in the limit $C\sigma_l \to 0$ is deduced from equation (3) as follows

$$I = \beta A L_P \int_{line} \tau(\lambda) d\lambda = \beta A L_P \tau_l \Delta\lambda_L . \tag{21}$$

Substituting τ_l from equation (19), equation (21) may be expressed as

$$\frac{I}{L_P \Delta\lambda_L} = \beta A N l\ 10^{-2} C\sigma_l , \tag{22}$$

where we see that the slope of this linear limit is the product *βA Nl*.

Substituting in equation (22) $10^{-2}CN$ from equation (11), σ_l from equation (18), then substituting k_t and r_i from equations (4) and (9) respectively, then calculating the product $L_P k_t$ and taking into account that the emission coefficient ($Wm^{-3}sr^{-1}$) is related to the line intensity in counts by $\varepsilon = I / \beta Al$, we arrive, after taking the natural logarithm, to the expression

$$\ln\left(\frac{\varepsilon\lambda_0}{A_{ki}g_k}\right) = -\frac{1}{kT}E_k + \ln\left(\frac{hcN_\alpha^z}{4\pi U^z(T)}\right). \quad (23)$$

Equation (23) shows that the linear limit of a $C\sigma$ graph leads, in a logarithmic plot, to the multi-element Boltzmann plots, described in [34] as a particular case of multi-element Saha-Boltzmann plots.

2.5 Plasma inhomogeneity, apparent parameters and validity of the plasma model

It is known that laser-induced plasmas are inhomogeneous, having spatial gradients of temperature, electron density and densities of atoms and ions present in the plasma. The temperature appearing in equations (1) and (2) is the local electron temperature in the plasma. As described in previous works [35,36], when the temperature is determined by means of Boltzmann diagrams constructed from the line intensity measured with spatial integration, an apparent temperature value is obtained, resulting from the integration of the emission coefficient within the region from which the emission of the spectrum occurs. Particularly, the apparent temperature measured with lines of neutral atoms is different from that obtained from lines of ions with a unit charge, given that the two ionization states occupy different regions of the plasma. The same occurs with electron density when it is obtained from the experimental profile measured with spatial integration [37]. In the same way, in the present work we consider that the parameters βA, Nl and T deduced from the fitting of a calculated $C\sigma$ curve to the experimental $C\sigma$ graph are apparent parameters, as this curve is obtained by integration of the equation of radiative transfer using a simple model of homogeneous plasma instead of the true complex inhomogeneous distribution of plasma parameters. Specifically, the temperature value which fits the experimental $C\sigma$ graph is the same as the apparent temperature resulting from the fitting to a straight line of the corresponding multi-element Boltzmann plot to which the $C\sigma$ graph approximates in the linear limit. Also, different apparent values for neutral atoms and ions of the columnar density Nl will be obtained as a result of the distinct distributions of neutral atom and ion densities. As a consequence, as happens with Boltzmann diagrams, two different $C\sigma$ graphs have to be considered, one for neutral atom lines and another for ion lines, each one leading to different values of the apparent parameters.

From the discussion in the previous paragraph, it is clear that $C\sigma$ curves calculated using the model of homogeneous plasma will not be able to provide accurately the ordinate of $C\sigma$ graphs for data corresponding to intense lines or high concentrations. This issue was already discussed for the case of conventional COGs in our previous work [21]. Our approach in the present work consists in using an homogeneous model in the integration of the equation of radiative transfer, whose simplicity is advantageous. This model is applied separately for neutral atoms and ions, so that different apparent parameters are deduced for the two ionization states. Moreover, a limit value for the validity of the model is introduced. We consider that this limit must be related to the quantity

$$\int_{line}\tau(\lambda)d\lambda = \tau_l\Delta\lambda_L = 10^{-2}C\ Nl\ k_t r_i. \quad (24)$$

Given a certain value of Nl, intense lines (high $k_t r_i$) or high concentrations (high $10^{-2}C$) will lead to a high value of $\tau_l\Delta\lambda_L$, exceeding a limit value $(\tau_l\Delta\lambda_L)_{\lim}$. The latter will be determined from the experiments, so that the data which are not well described can be eliminated from the $C\sigma$ graphs.

3. Experiment

The experimental system is similar to that used in previous works [38,39], so it will only be described briefly. Laser-induced plasmas are generated focusing a Nd:YAG laser (wavelength 1064 nm, pulse energy 60 mJ, pulse width 4.5 ns, repetition rate 20 Hz) onto the surface of the samples in air at atmospheric pressure.The laser beam is perpendicular to the sample surface, the focusing lens has 126 mm focal length and the lens-to-sample distance is 122 mm. The emission of the plasma is collected in a direction forming a small angle with the laser beam by a system of flat and concave mirrors forming a 1:1 image of the plasma on the entrance slit of a 0.75-m Czerny-Turner spectrometer equipped with a time-resolved intensified CCD (1200 × 256 effective pixels). The grating and the slit width are selected according to the spectral resolution needed. A grating of 3600 lines mm^{-1} and a slit width of 20 µm are used in the measurement of spectra for $C\sigma$ graphs while, for electron density determination, the spectrum of the H_α line is obtained with a grating of 1200 lines mm^{-1} and a slit of 50 µm. The instrumental width was determined as 0.135 Å from the profile of emission lines measured at late times of the plasma lifetime, when the electron density becomes low. This instrumental width is low

enough to resolve the spectra measured in this work. The line intensities are determined by fitting the lines to Voigt profiles. During the measurements, the emission of 100 laser shots is accumulated while the sample rotates at 100 rev min^{-1}. The measured spectra are corrected by the spectral efficiency of the system, whose spectral response is measured using calibrated deuterium and tungsten lamps.

The samples are fused glass disks prepared by fusion of oxides in borate mixtures. The oxides used are high purity Fe_2O_3, Cr_2O_3, MnO_2, MgO and SiO_2 in powder form. Table 1 shows the element content in the samples A-E, expressed in per cent atomic concentrations (at. %).

4. Results and discussion

4.1 Cσ graphs for Fe II and Fe I lines

Iron has been selected as the element to begin the experimental study of *Cσ* graphs due to the high number of Fe I and Fe II transitions with known transition probabilities. In Table 2, the lines use to construct the *Cσ* graphs are listed, together with their atomic data, including the Stark widths, when available. The Stark width data have been normalized to an electron density $N_e = 10^{17}$ cm^{-3} and the width for a temperature as close as possible to the plasma temperature has been chosen. For the lines for which the uncertainty of the Stark width is not provided in the table, the experimental Stark width is not available, and the average of known Stark widths for lines of the same multiplet has been used. In the case of Fe I, few experimental Stark widths are available. For the Fe I lines in the table without a value, an estimated Stark width $w = 0.1\times10^{-17}$ Å cm^3 has been used taking into account that, as discussed later, the effect of the Lorentzian width on the *Cσ* graph is not relevant in this particular case.

A time window with a delay of 2.6 μs and a width of 0.8 μs has been used to measure the Fe II and Fe I spectra emitted by the plasma generated with sample A. As done in previous works [38,39], in all the experiments performed here the electron density of the plasma has been measured from the Stark broadening of the H_α line, using the diagnosis tables reported by Gigosos and Cardeñoso [42]. The resulting value of the electron density is shown in Table 3, together with the values of other plasma parameters. In the case of the electron density, a single value has been considered at a given time window for both the neutral atom and ion lines. Using this value and typical values of temperature for neutral atoms and ions, initial values of σ_l for the Fe I and Fe II lines are obtained from which the abscissas of the *Cσ* graphs are deduced. On the other side, the ordinates are obtained by measuring the line intensities and calculating L_P for each line. The intensities are measured by fitting the lines to Voigt profiles. When the *Cσ* graphs for Fe II and Fe I are constructed, the data do not show a smooth behaviour, as the abscissa of the graphs depends on temperature trough the line cross section σ_l and the typical temperature introduced is possibly far from the true value, thereby displacing the abscissa from the correct value. To obtain an estimation of the temperature, a Boltzmann plot may be built from the data having a low abscissa in the *Cσ* graph, for which self-absorption is small. The resulting Boltzmann plots for Fe II and Fe I, shown in Fig. 3, have different slopes, corresponding to the distinct apparent temperatures for neutral atoms and ions. If these temperatures are used to calculate σ_l and L_P, the *Cσ* graphs shown in Fig. 4 are obtained. The experimental graphs have been fitted to *Cσ* curves with the result shown in the figure. From the fittings, the parameters βA, Nl and the product $\beta A\ Nl$ are obtained, whose values and standard deviations are shown in Table 3. It is worth mentioning that the apparent temperature may also be obtained from the fitting of the *Cσ* graphs to *Cσ* curves, a process in which each iteration step leads to the mentioned shift of the temperature-dependent abscissas of the data. For the Fe II curve (Fig. 4a), the linear limit of slope $\beta A\ Nl$ is also shown in the figure. The departure of the data from the linear limit reflects the self-absorption of the Fe II lines. For its part, the self-absorption is not noticeable in the *Cσ* graph of Fe I (Fig 4b) and, as a consequence, the parameters βA, Nl are undetermined while the product $\beta A\ Nl$ can be obtained by fitting the graph. Furthermore, the only effect of changing the Lorentzian width $\Delta\lambda_L$ for the data in a linear *Cσ* graph such as that of Fig. 4b is to multiply the abscissa and the ordinate by the same factor. This means that an error in the Stark width does not affect the slope of the linear region of a *Cσ* graph, causing only a displacement of the data along the curve. On the other side, for data in the non-linear region of *Cσ* graphs as that of Fig. 4a, an inaccurate Stark width leads to a departure of the ordinate from the general *Cσ* curve, which worsens the correlation of the fitting. The relevance of this effect increases with the degree of self-absorption. Thus, in the case of moderate to high self-absorption, accurate Stark width data are necessary for the use of *Cσ* graphs.

From the temperature and the electron density, the values of k_t and σ_l for any line may be obtained, provided that its atomic data, including the Stark width, are known. The k_t and σ_l values for the lines used to construct the *Cσ* graphs of Fig. 4 are shown in Table 2. These values are useful to classify the lines in terms of their intensity, normalized to L_P, in the optically thin limit (k_t for a given element or $k_t r_i$ taking into account the ionization of different elements) and self-absorption (σ_l) for a given concentration and value of the Nl parameter.

4.2 Cσ graphs for several elements

To verify experimentally the applicability of *Cσ* graphs for several elements, samples B and C have been used. As a single sample is used to obtain each of the *Cσ* graphs, only the absence of a matrix effect affecting the stoichiometry is required for their validity. For ions, a *Cσ* graph has been obtained using sample B, including the Fe II lines of Table 2 and also the Mn II and Mg II lines listed in Table 4. The time delay used in this case is 1.15 μs and the time width, 0.3 μs. The experimental *Cσ* graph, together with the fitting *Cσ* curve, is shown in Fig. 5. The data with a low abscissa in the *Cσ* graph lead, as mentioned before, to a multi-element Boltzmann plot, shown in Fig. 6. The temperature is obtained from the slope of this plot; the same value, within the experimental error, is deduced from the fitting of the *Cσ* graph. The electron density N_e, the parameters βA, Nl, T and the product $\beta A\ Nl$ resulting from the fitting are shown in Table 3. To obtain the graph and the curve in Fig. 5, the ionization factor r_i has been calculated from the T and N_e values. The value of r_i is high for the three elements (0.978 for Fe, 0.984 for Mn and 0.968 for Mg), showing the high ionization of the plasma at the time window selected. As can be seen in Fig. 5, the data of the *Cσ* graph show a smooth behaviour and there is a high correlation to the *Cσ* curve.

To obtain a *Cσ* graph for neutral atoms, sample C and a time window with a 3-μs delay and 1-μs width have been used. The Fe I lines of Table 2, together with Si I lines listed in Table 5, have been included. Fig. 7 shows the experimental *Cσ* graph and the fitting *Cσ* curve. Table 3 shows the electron density and the parameters deduced from the fitting. For the nearly linear graph in Fig. 7, the parameters βA, Nl are again undetermined, so only the product $\beta A\ Nl$ is provided.

4.3 Cσ graphs for several elements and concentrations

Using several samples, *Cσ* graphs may be constructed including various lines of different species (atoms or ions of several elements) at varying concentrations. In this case, an absence of matrix effects affecting the stoichiometry or the plasma parameters is required. To verify this experimentally, we have used samples D and E, containing different concentrations of Fe and Cr. The lines included are the Fe II lines of Table 2 and the Cr II lines in Table 6. The time delay and width are 1.15 and 0.3 μs, respectively. The experimental *Cσ* graph and the fitting *Cσ* curve are shown in Fig. 8. As can be seen, the data are well described by a single *Cσ* curve. However, a deviation of the ordinates of the Cr data from those of Fe, slightly higher than the experimental error, is observed. We attribute this deviation to a small disagreement of the average concentration of chromium in samples D and E, compared to the nominal value listed in Table 1. This disagreement may be explained by the small solubility of chromium oxide in lithium borates [52], which causes some crystallization, leading to a lower average concentration in the fused glass sample. The parameters βA, Nl, T and the product $\beta A\ Nl$ resulting from the fitting of the plot in Fig. 8 are shown in Table 3, together with the electron density. The existence of a single *Cσ* graph, described by a unique set of plasma parameters but obtained from various samples, supports the assumption of the absence of matrix effects.

4.4 Limit of validity of the homogeneous plasma model

As mentioned in subsection 2.5, the simple model of an homogeneous plasma is not expected to be valid to describe the ordinate of data of *Cσ* graphs in the case of intense lines or high concentrations. It has been verified experimentally that intense lines as the resonance Mg II line at 2802.705 Å ($k_t = 189.8\times10^{-20}$ m^2 Å at 14000 K) appear well below the *Cσ* curve of less intense lines. Also, it has been checked that the data of the *Cσ* graphs are outside the *Cσ* curve if the concentration is significantly increased. In the experiments performed in this work, we have found that a limit of validity of the homogeneous plasma model may be established using $\left(\tau_l \Delta\lambda_L\right)_{\lim} \cong 0.1$ Å as, using data with $\tau_l \Delta\lambda_L$ lower than this limit, the resulting *Cσ* graphs are smooth and may be fitted to *Cσ* curves, as shown in Figs. 4, 5, 7 and 8.

4.5 Plasma parameters

The plasma parameters, shown in Table 3 together with their standard deviations and ordered according to the delay used, are interpreted in this subsection. The electron density is in all cases above the critical value for existence of LTE according to McWhirter criterion [53]. Moreover, the smooth behavior of the experimental *Cσ* graphs and their high correlation to *Cσ* curves also support the assumption of LTE, as the latter are based on the Boltzmann, Saha and radiative transfer equations. In Table 3 we observe that, in the case of ions in which two *Cσ* graphs have been obtained for the same time window, the parameters Nl, T and N_e coincide within the errors. This observation is a verification of the absence of matrix effects for the samples used. As can be seen, the electron density N_e and temperature T decrease for increasing delay, as expected from the expansion and cooling of the plasma. On the contrary, the columnar density Nl for ions is the same within the error at 1.15 μs and 2.6 μs delays. This experimental observation may be related to the combined effect of a decrease in the total density N and increase of the length l of the plasma along the line of sight, both effects being due to expansion. However, the interpretation of the behaviour of the columnar density Nl has to be made with care, as this is an apparent parameter dependent on the true spatial distribution of emitting species, which

will suffer a complex temporal evolution. With respect to the βA parameter, its interpretation is even more difficult since the instrumental factor β depends on the time gate used and on the gain of the microchannel plate of the image intensifier, and both instrumental parameters have been modified in the experiments. Moreover, the transverse area A needs not to be equal for neutral atoms and ions and will also depend on the delay due to expansion. However, if $C\sigma$ graphs are measured using a given microchannel plate gain and time window, it is expected that the LIBS system will be characterized by two stable values of βA, one for neutral atoms and the other for ions. We have checked that the βA parameters obtained in measurements of $C\sigma$ graphs carried out in different days are rather stable. Therefore, the results of this work prompt the idea of using $C\sigma$ graphs to characterize a LIBS system by a set of parameters βA, Nl, T, N_e, each one having different values for neutral atoms and ions. Among these parameters, βA is mainly characteristic of the instrument through the β factor, while Nl, T, N_e characterize the plasma. From the parameters, two $C\sigma$ curves may be calculated, which allow predicting the intensity of a line of a given element and ionization state at a certain concentration, as well as the degree of self-absorption it will experience, provided that accurate atomic data are available and the limit of validity of the model is not exceeded.

5. Conclusions

A new approach for characterization of laser-induced plasmas in LIBS experiments is presented. The method is based on experimental $C\sigma$ graphs, which allow including several lines of various elements at different concentrations in the characterization process. $C\sigma$ graphs rely in the calculation of a line cross section σ_l for the experimental data. This parameter, which depends on the temperature and electron density of the plasma, is obtained from the atomic data of line, including the oscillator strength or transition probability and the Stark width. It includes the three factors influencing the optical depth of a given line, i.e., the k_t coefficient, the ionization factor r_i and the factor $1/\Delta\lambda_L$, accounting for the line shape. The line cross section is useful to compare the optical depth of spectral lines of different line widths emitted by elements with different ionization energies. After fitting $C\sigma$ graphs to calculated $C\sigma$ curves, the LIBS system and the plasma are characterized by a set of four apparent parameters βA, Nl, T, N_e, having different values for neutral atom and ion lines. A limit of validity for the model of plasma used exists, allowing to discard data corresponding to intense lines or high concentrations during the construction of $C\sigma$ graphs. Starting from the parameters, the intensity of a line and its self-absorption may be predicted from its atomic data, provided that the limit of validity is not exceeded. Three versions of the $C\sigma$ graph have been proposed: (1) A graph including lines of a single species (atom or ion) having enough transitions with available atomic data (e.g. Fe I and Fe II) is valid for determining the apparent parameters for the corresponding ionization state, provided that self-absorption is present in the graph for the lines and concentration used. (2) Determination of the parameters may also be performed constructing a $C\sigma$ graph which includes lines of several elements. This is a useful procedure for a sample containing elements which have few emission lines for a given ionization stage. It is worth stressing that these two versions of $C\sigma$ graphs provide characterization using a single sample and therefore require only the stoichiometry condition, the method being valid even if a matrix effect affecting the plasma parameters exists. (3) In cases in which, even including several elements, there are few lines available for an accurate determination of the parameters, a $C\sigma$ graph may be obtained using samples with different concentrations. In this procedure, the graph corresponding to a line of one of the elements is equivalent to a conventional COG. This version of the $C\sigma$ graph requires that the plasma parameters are not affected by the variation of the sample composition. For the three versions of $C\sigma$ graphs, if the available lines and concentrations lead only to optically thin data, the columnar density Nl remains undetermined, and the linear fitting of the graphs provides the product βANl and the temperature. The existence of the tree versions of $C\sigma$ graphs for neutral atoms and ions has been experimentally verified.

Acknowledgement

This work has been supported by the project FIS2011-29521 of the Spanish Ministerio de Economía y Competitividad.

References

[1] Aragón C, Aguilera JA. Characterization of laser induced plasmas by optical emission spectroscopy: A review of experiments and methods. Spectrochim Acta Part B 2008;63:893-916.
[2] Hahn DW, Omenetto N. Laser-induced breakdown spectroscopy (LIBS), part I: Review of basic diagnostics and plasma-particle interactions: Still-challenging issues within the analytical plasma community. Appl Spectrosc 2010;64:335A-366A.
[3] Radziemski LJ, Loree TR, Cremers DA, Hoffman NM. Time-resolved laser-induced breakdown spectrometry of aerosols. Anal Chem 1983;55: 1246-1252.
[4] Simeonsson JB, Miziolek AW. Time-resolved emission studies of ArF-laser-produced microplasmas. Appl Opt 1993;32: 939-947.

[5] Sabsabi M, Cielo P. Quantitative analysis of aluminium alloys by laser-induced breakdown spectroscopy and plasma characterization. Appl Spectrosc 1995;49: 499-507.
[6] Bulajic D, Corsi M, Cristoforetti G, Legnaioli S, Palleschi V, Salvetti A, Tognoni E. A procedure for correcting self-absorption in calibration free-laser induced breakdown spectroscopy. Spectrochim Acta Part B 2002;57: 339-353.
[7] Amamou H, Bois A, Ferhat B, Redon R, Rosetto B, Ripert M. Correction of the self-absorption for reversed spectral lines: application to two resonance lines of neutral aluminum. J Quant Spectr Radiat Transfer 2003;77:365-372.
[8] El Sherbini AM, El Sherbini ThM, Hegazy H, Cristoforetti G, Legnaioli S, Palleschi V, Pardini L, Salvetti A, Tognoni E, Evaluation of self-absorption coefficients of aluminum emission lines in laser-induced breakdown spectroscopy measurements. Spectrochim Acta Part B 2005;60: 1573-1579.
[9] Díaz-Pace DM, D'Angelo CA, Bertuccelli G. Calculation of optical thicknesses of magnesium emission spectral lines for diagnostics of laser-induced plasmas. Appl Spectrosc 2011;65:1202-1212.
[10] Moon H-Y, Herrera KK, Omenetto N, Smith BW, Winefordner JD. On the usefulness of a duplicating mirror to evaluate self-absorption effects in laser induced breakdown spectroscopy. Spectrochim Acta Part B 2009;64:702-713.
[11] Hermann J, Boulmer-Leborgne C, Hong D. Diagnostics of the early phase of an ultraviolet laser induced plasma by spectral line analysis considering self-absorption. J Appl Phys 1998;83:691-696.
[12] D'Angelo C, Díaz-Pace DM, Bertuccelli G, Bertuccelli D. Laser induced breakdown spectroscopy on metallic alloys: Solving inhomogeneous optically thick plasmas 2008;63: 367-374.
[13] D'Angelo CA, Díaz-Pace DM, Bertuccelli G. Semiempirical model for analysis of inhomogeneous optically thick laser-induced plasmas. Spectrochim Acta Part B 2009;64:999-1008.
[14] Wester R, Noll R. Heuristic modeling of spectral plasma emission for laser-induced breakdown spectroscopy. J Appl Phys 2009;106:123302 (10p).
[15] Gornushkin IB, Stevenson CL, Smith BW, Omenetto N, Winefordner JD. Modeling an inhomogeneous optically thick laser induced plasma: a simplified theoretical approach. Spectrochim Acta Part B 2001; 56:1769-1785.
[16] Gornushkin IB, Omenetto N, Smith BW, Winefordner JD. Determination of the maximum temperature at the center of an optically thick laser-induced plasma using self-reversed spectral lines. Appl Spectrosc 2004;58: 1023-1031.
[17] Cristoforetti G, Tognoni E. Calculation of elemental columnar density from self-absorbed lines in laser-induced breakdown spectroscopy: A resource for quantitative analysis. Spectrochim Acta Part B 2013;79-80:63-71.
[18] Gornushkin IB, Anzano JM, King LA, Smith BW, Omenetto N, Winefordner JD. Curve of growth methodology applied to laser-induced plasma emission spectroscopy. Spectrochim Acta Part B 1999;54:491-503.
[19] Lazic V, Barbini R, Colao F, Fantoni R, Palucci A. Self-absorption model in quantitative laser induced breakdown spectroscopy measurements on soils and sediments. Spectrochim Acta Part B 2001; 56:807-820.
[20] Aragón C, Bengoechea J, Aguilera JA. Influence of the optical depth on spectral line emission from laser-induced plasmas. Spectrochim Acta Part B 2001;56:619-628.
[21] Aguilera JA, Bengoechea J, Aragón C. Curves of growth of spectral lines emitted by a laser-induced plasma: influence of the temporal evolution and spatial inhomogeneity of the plasma. Spectrochim. Acta Part B 2003;58:221-237.
[22] Aragón C, Peñalba F, Aguilera JA. Curves of growth of neutral atom and ion lines emitted by a laser induced plasma. Spectrochim. Acta Part B 2005;60:879-887.
[23] Aguilera JA, Aragón C. Characterization of laser-induced plasmas by emission spectroscopy with curve-of-growth measurements. Part I: Temporal evolution of plasma parameters and self-absorption. Spectrochim Acta Part B 2008;63:784-792.
[24] Acquaviva S, D'Anna E, De Giorgi ML, Moro F. Laser-induced breakdown spectroscopy for compositional analysis of multielemental thin films. Spectrochim Acta Part B 2006;61:810-816.
[25] Balzer H, Hölters S, Sturm V, Noll R. Systematic line selection for online coating thickness measurements of galvanised sheet steel using LIBS. Anal Bioanal Chem 2006;385:234-239.
[26] Peter L, Noll R. Material ablation and plasma state for single and collinear double pulses interacting with iron samples at ambient gas pressures below 1 bar. Appl Phys B 2007;86:159-167.
[27] Sturm V, Schmitz H-U, Reuter T, Fleige R, Noll R. Fast vacuum slag analysis in a steel works by laser-induced breakdown spectroscopy. Spectrochim Acta Part B 2008;63:1167-1170.
[28] Estupiñán H, Peña DY, García YO, Cabanzo R, Mejía-Ospino E. Stoichiometry analysis of titanium oxide coating by LIBS. Eur Phys J D 2009;53:69-73.
[29] Griem HR. Plasma spectroscopy. New York: McGraw-Hill; 1964.
[30] Thorne A, Litzén U, Johansson S. Spectrophysics: Principles and applications. Berlin: Springer; 1999.
[31] Kuntz M. A new implementation of the Humlicek algorithm for the calculation of the Voigt profile function. J Quant Spectrosc Radiat Transfer 1997;57:819-824.

[32] Zel'dovich YB, Raizer Y. Physics of shock waves and high-temperature hydrodynamic phenomena. New York: Dover Publications Inc; 2002.
[33] Hinnov E. A method of determining optical cross sections. J Opt Soc Am 1957;47:151-155.
[34] Aguilera JA, Aragón C. Multi-element Saha-Boltzmann and Boltzmann plots in laser-induced plasmas. Spectrochim Acta Part B 2007;62:378-385.
[35] Aguilera JA, Aragón C. Characterization of a laser-induced plasma by spatially resolved spectroscopy of neutral atom and ion emissions. Comparison of local and spatially integrated measurements. Spectrochim Acta Part B 2004;59:1861-1876.
[36] Aguilera JA, Aragón C. Apparent excitation temperature in laser-induced plasmas. J Phys C: Conf Ser 2007;59:210-217.
[37] Aragón C, Aguilera JA. Determination of the local electron number density in laser-induced plasmas by Stark-broadened profiles of spectral lines. Comparative results from Hα, Fe I and Si II lines. Spectrochim Acta Part B 2010;65:395-400.
[38] Aguilera JA, Manrique J, Aragón C. Stark width measurements of FeII lines with wavelengths in the range 230–260 nm. J Phys B At Mol Opt Phys 2011;44:245701(6p).
[39] Aragón C, Aguilera JA, Manrique J. Measurement of Stark broadenig parameters of FeII and NiII spectral lines by laser induced breakdown spectroscopy using fused glass samples. J Quant Spectr Radiat Transfer 2014; 134:39-45.
[40] Fuhr JR,Wiese WL. A critical compilation of atomic transition probabilities for neutral and singly ionized iron. J Phys Chem Ref Data 2006;35:1669-1809.
[41] Aragón C, Vega P, Aguilera JA. Stark width measurements of Fe II lines with wavelengths in the range 260-300 nm. J. Phys B:At Mol Opt Phys 2011;44: 055002 (7pp).
[42] Gigosos MA, Cardeñoso V. New plasma diagnosis tables of hydrogen Stark broadening including ion dynamics. J Phys B:At Mol Opt Phys 1996;29:4795-4838.
[43] Kramida A, Ralchenko Yu, Reader J and NIST ASD Team. NIST Atomic Spectra Database (ver. 5.1), [Online] 2013; Available: http://physics.nist.gov/asd.
[44] Kling R, Griesmann U. Accurate f-values for ultraviolet transitions from the $3d^5(^6S)4p$ levels in Mn II. Astrophys J 2000;531:1173-1178.
[45] Bukvić S, Srećković A, Djeniže S. Mg II h and k lines Stark parameters. New Astron 2004;9:629-633.
[46] Djeniže S, Bukvić S, Srećković A, Platiša M. Mg II spectral line broadening in helium, oxygen and argon-helium plasmas. Astron & Astrophys 2004;424:561-564.
[47] Djeniže S, Bukvić S, Srećković A, Nikolić. The first measured Mn II and Mn III Stark broadening parameters. New Astron 2006;11:256-261.
[48] Kelleher DE, Podobedova LI. Atomic Transition Probabilities of Silicon. A Critical Compilation. J Phys Chem Ref Data 2008; 37:1285-1501.
[49] Bukvić S, Djeniže S, Srećković A. Line broadening in the Si I, Si II, Si III, and Si IV spectra in helium plasma. Astron & Astrophys 2009;508:491-500.
[50] Nilsson H, Ljung G, Lunberg H, Nielsen KE. The FERRUM project: improved experimental oscillator strengths in Cr II. Astron & Astrophys 2006;445:1165-1168.
[51] Aguilera JA, Aragón C, Manrique J. Experimental Stark widths and shifts of Cr II spectral lines. Mon Not R Astron Soc 2014;438:841-845.
[52] Claisse F. Choix de la composition optimale d'un borate de lithium dans la préparation des perles pour analyses par fluo-X. J Phys IV France 1998;8:379-384.
[53] McWhirter RWP, Spectral intensities, in: Huddlestone RH, Leonard SL (Eds.), Plasma diagnostic techniques, New York: Academic Press; 1965, Chapter 5.

Tables

Table 1. Composition of fused glass samples.

	Concentration (at.%)				
Sample	Fe	Mg	Mn	Si	Cr
A	0.200				
B	0.200	0.050	0.030		
C	0.400			0.101	
D	0.100				0.050
E	0.201				0.100

Table 2. Fe II and Fe I lines used to construct the $C\sigma$ graphs, with their atomic data and typical k_t and σ_l values.

	λ_0 (Å)	E_i (eV)	E_k (eV)	g_i	g_k	A_{ki}[a] (10^8 s^{-1})	f[a]	Acc.	w (Å)	Acc.	k_t[b] (10^{-20} m^{2}Å)	σ_l[c] (10^{-20} m^2)
Fe II	2368.596	0.35	5.58	6	4	0.606	0.034	B+	0.047[d]	15	0.804	6.66
	2373.736	0.00	5.22	10	10	0.425	0.0359	B+	0.042[e]	15	1.90	17.6
	2375.193	0.39	5.60	4	2	0.981	0.0415	B	0.051[d]	15	0.639	4.88
	2382.039	0.00	5.20	10	12	3.13	0.32	B+	0.038[e]	15	17.1	175
	2391.478	0.30	5.48	8	10	0.0377	0.00405	B	0.049	-	0.136	1.09
	2395.626[f]	0.05	5.22	14	14	1.926	0.16609	B+	0.040	-	12.1	117
	2404.887	0.08	5.24	6	8	1.96	0.227	B+	0.043[d]	15	6.91	62.6
	2410.520	0.11	5.25	4	6	1.55	0.203	B+	0.0431[e]	15	4.06	36.6
	2411.069	0.12	5.26	2	2	2.37	0.207	B+	0.041[e]	15	2.05	19.4
	2430.079	2.83	7.93	8	10	1.91	0.211	C+	0.044[e]	15	0.898	7.94
	2432.262	2.84	7.94	6	8	1.57	0.186	C+	0.043[e]	15	0.587	5.31
	2439.302	3.15	8.23	12	14	2.25	0.234	C	0.039[e]	15	1.15	11.5
	2444.516	2.58	7.65	6	8	2.78	0.332	C	0.046[e]	15	1.31	11.1
	2585.876	0.00	4.79	10	8	0.894	0.0717	B+	0.0411[e]	15	4.48	42.5
	2591.543	1.04	5.82	6	6	0.572	0.0576	B	0.047[d]	15	0.916	7.59
	2592.785	4.08	8.86	14	16	2.74	0.316	C	0.045[e]	15	0.948	8.20
	2598.370	0.05	4.82	8	6	1.43	0.108	B+	0.039	-	5.24	51.6
	2599.396	0.00	4.77	10	10	2.35	0.239	B+	0.045[d]	15	15.1	131
	2611.874	0.05	4.79	8	8	1.2	0.122	B+	0.0368[g]	14	5.98	63.3
	2617.618	0.08	4.82	6	6	0.488	0.0501	B	0.038[d]	15	1.80	18.4
	2730.734	1.08	5.62	4	4	0.279	0.0313	B	0.050[g]	14	0.356	2.77
	2736.966	1.08	5.60	4	2	1.22	0.0685	B	0.054	-	0.783	5.68
	2739.548	0.99	5.51	8	8	2.21	0.249	B+	0.0534[g]	14	6.14	44.8
	2743.197	1.10	5.62	2	4	1.97	0.445	B+	0.0515[g]	14	2.51	19.0
	2746.484	1.08	5.59	4	6	2.05	0.348	B	0.054[g]	14	4.00	28.9
	2746.982	1.04	5.55	6	6	1.69	0.191	B	0.056[g]	14	3.40	23.6
	2753.288	3.27	7.77	10	12	1.89	0.258	C	0.0532[g]	14	1.21	8.87
	2755.737	0.99	5.48	8	10	2.15	0.306	B	0.0540[g]	14	7.63	55.0
Fe I	3734.864	0.86	4.18	11	11	0.901	0.189	A	0.08	-	14.2	12.1
	3749.485	0.91	4.22	9	9	0.763	0.161	A	0.08	-	9.41	7.99
	3758.233	0.96	4.26	7	7	0.634	0.134	A	0.08	-	5.85	4.96
	3763.789	0.99	4.28	5	5	0.544	0.116	A	0.08[h]	20	3.50	2.98
	3765.539	3.24	6.53	13	15	0.951	0.233	B+	0.07[h]	20	1.71	1.66
	3767.192	1.01	4.30	3	3	0.639	0.136	A	0.08[h]	20	2.42	2.05
	3795.002	0.99	4.26	5	7	0.115	0.0347	A	0.08	-	1.06	0.904
	3797.515	3.24	6.50	13	13	0.457	0.0989	B+	-	-	0.739	0.502
	3805.342	3.30	6.56	9	11	0.86	0.228	B+	0.07	-	1.11	1.07
	3815.840	1.48	4.73	9	7	1.12	0.19	A	0.11[h]	20	6.29	3.89
	3820.425	0.86	4.10	11	9	0.667	0.12	A	0.09[i]	20	9.42	7.11
	3821.178	3.27	6.51	11	13	0.554	0.143	B+	0.07	-	0.885	0.859
	3827.822	1.56	4.80	7	5	1.05	0.165	A	0.14[i]	20	3.96	1.92
	3834.222	0.96	4.19	7	5	0.452	0.0713	A	0.09	-	3.230	2.44
	3856.372	0.05	3.27	7	5	0.0464	0.00739	A	0.09[i]	20	0.881	0.665
	3859.212	2.40	5.62	13	11	0.0725	0.0137	B+	-	-	0.254	0.172
	3859.912	0.00	3.21	9	9	0.0969	0.0217	A	0.11[i]	20	3.51	2.17
	3865.523	1.01	4.22	3	3	0.155	0.0347	A	0.09	-	0.647	0.488
	3872.501	0.99	4.19	5	5	0.105	0.0236	A	0.09	-	0.752	0.568
	3873.760	2.43	5.63	11	9	0.0657	0.0121	B+	-	-	0.185	0.126

[a]Data from Ref. [40].
[b]Calculated for T = 14000 K (Fe II), T = 11000 K (Fe I).
[c]Calculated for T = 14000 K, $N_e = 2.5\times10^{17}$ cm^{-3} (Fe II); T = 11000 K, $N_e = 10^{17}$ cm^{-3} (Fe I).
[d]Data from Ref. [39].
[e]Data from Ref. [38].
[f]The lines at 2395.420 Å and 2395.626 Å have been grouped, and the resulting data are indicated.
[g]Data from Ref. [41].
[h]Data from Ref. [23].
[i]Data from Ref. [22].

Table 3. Experimental conditions (sample used, delay and width of the time window) and fitting parameters for each $C\sigma$ graph obtained in this work.

	Figure	Sample	Delay (μs)	Width (μs)	βA (cntsW^{-1}m^{2}sr)	Nl (10^{20} m^{-2})	βANl (10^{20} cntsW^{-1}sr)	T (10^3 K)	N_e[a] (10^{17} cm^{-3})
Ion	5	B	1.15	0.3	850 ± 100	3.6 ± 0.4	3030 ± 50	14.4 ± 0.2	2.49
	7	D, E	1.15	0.3	2200 ± 300	3.2 ± 0.4	6960 ± 90	14.4 ± 0.3	2.46
	4a	A	2.6	0.8	4800 ± 500	3.3 ± 0.3	15900 ± 400	12.4 ± 0.2	1.07
Neutral	4b	A	2.6	0.8	-	-	16700 ± 300	10.6 ± 0.3	1.07
	6	C	3	1	-	-	13700 ± 400	9.6 ± 0.2	0.91

[a]The estimated relative error is 11%.

Table 4. Mg II and Mn II lines used to construct the $C\sigma$ graph, with their atomic data and typical k_t and σ_l values.

	λ_0 (Å)	E_i (eV)	E_k (eV)	g_i	g_k	A_{ki} (10^8 s^{-1})	f	Acc.	w (Å)	Acc.	k_t[g] (10^{-20} m^2Å)	σ_l[h] (10^{-20} m^2)
Mg II	2790.777	4.42	8.86	2	4	4.01[b]	0.9370	A	0.161[d]	B+	14.90	35.68
	2797.998[a]	4.43	8.86	8	10	3.193[b]	0.4689	A	0.143[d]	B+	29.69	80.05
	2928.633	4.42	8.65	2	2	1.15[b]	0.1480	A	0.29[e]	B+	2.58	3.43
	2936.510	4.43	8.65	4	2	2.3[b]	0.1490	A	0.3[e]	B+	5.17	6.64
Mn II	2576.105	0.00	4.81	7	9	2.82[c]	0.3609	1%	0.143	-	52.08	142.78
	2593.724	0.00	4.78	7	7	2.77[c]	0.2795	4%	0.14[f]	16%	40.86	114.44
	2605.684	0.00	4.76	7	5	2.72[c]	0.1979	4%	0.147[f]	16%	29.19	77.85
	2933.055	1.17	5.40	5	3	2.01[c]	0.1556	5%	0.163[f]	16%	7.76	18.67
	2939.308	1.17	5.39	5	5	1.95[c]	0.2527	4%	0.121[f]	16%	12.65	41.00
	2949.205	1.17	5.38	5	7	1.94[c]	0.3544	4%	0.16[f]	16%	17.86	43.76

[a]The lines at 2797.930 Å and 2797.998 Å have been grouped, and the resulting data are indicated.
[b]Data from Ref. [42].
[c]Data from Ref. [43].
[d]Data from Ref. [44].
[e]Data from Ref. [45].
[f]Data from Ref. [46].
[g]Calculated for T = 14000 K.
[h]Calculated for T = 14000 K, $N_e = 2.5 \times 10^{17}$ cm^{-3}.

Table 5. Si I lines used to construct the $C\sigma$ graph, with their atomic data and typical k_t and σ_l values.

	λ_0 (Å)	E_i (eV)	E_k (eV)	g_i	g_k	A_{ki}[a] (10^8 s^{-1})	f	Acc.	w (Å)	Acc.	k_t[b] (10^{-20} m^2Å)	σ_l[c] (10^{-20} m^2)
Si I	2210.892	0.01	5.62	3	5	0.346	0.0423	B	0.061[d]	38	4.50	12.2
	2216.669	0.03	5.62	5	7	0.454	0.0469	B	0.063	-	8.21	21.6
	2506.897	0.01	4.95	3	5	0.547	0.0859	B	0.141[d]	29	11.7	13.8
	2516.112	0.03	4.95	5	5	1.68	0.1590	B	0.117[d]	31	35.8	50.7
	2528.508	0.03	4.93	5	3	0.904	0.0520	B	0.107[d]	35	11.8	18.3
	2881.578	0.78	5.08	5	3	2.17	0.1620	B	0.145[d]	28	21.5	24.6

[a]Data from Ref. [48].
[b]Calculated for T = 11000 K.
[c]Calculated for T = 11000 K, $N_e = 10^{17}$ cm^{-3}.
[d]Data from Ref. [49].

Table 6. Cr II lines used to construct the $C\sigma$ graph, with their atomic data and typical k_t and σ_l values.

	λ_0 (Å)	E_i (eV)	E_k (eV)	g_i	g_k	A_{ki}[b] (10^8 s^{-1})	f	Acc.	w[c] (Å)	Acc.	k_t[d] (10^{-20} m^2Å)	σ_l[e] (10^{-20} m^2)
Cr II	2055.596	0.00	6.03	6	8	1.29	0.1090	9	0.037	15	6.32	67.14
	2061.575	0.00	6.01	6	6	1.28	0.0816	9	0.034	15	4.76	55.01
	2653.578	1.49	6.16	4	6	0.381	0.0604	6	0.053	15	1.11	8.26
	2668.707	1.49	6.14	4	2	1.45	0.0775	8	0.046	15	1.45	12.34
	2671.803	1.51	6.15	6	4	1.09	0.0778	7	0.046	15	2.16	18.41
	2672.826	1.53	6.16	8	6	0.574	0.0461	6	0.054	15	1.68	12.20
	2677.159[a]	1.54	6.17	18	18	1.69	0.1817	-	0.046	0	14.76	126.12
	2678.789	1.49	6.12	4	6	0.802	0.1295	7	0.05	15	2.43	19.11
	2751.864	1.53	6.03	8	8	0.557	0.0633	9	0.048	15	2.43	19.93
	2757.720	1.51	6.00	6	4	0.997	0.0758	9	0.047	15	2.23	18.65
	2762.589	1.53	6.01	8	6	1.59	0.1365	9	0.045	15	5.29	46.18
	2766.531	1.55	6.03	10	8	2.23	0.2048	9	0.044	15	9.75	87.08
	2835.629	1.55	5.92	10	12	2.5	0.3619	3	0.05	15	18.06	141.93
	2843.249	1.53	5.89	8	10	1.89	0.2865	3	0.051	15	11.73	90.34
	2849.837	1.51	5.86	6	8	1.52	0.2469	3	0.051	15	7.74	59.60
	2860.934	1.48	5.82	2	4	0.724	0.1778	5	0.05	15	1.91	14.98
	2862.571	1.53	5.86	8	8	0.866	0.1064	5	0.047	15	4.41	36.88
	2870.432	2.45	6.77	6	6	0.955	0.1180	10	0.065	15	1.71	10.32
	3118.646	2.42	6.40	2	4	1.36	0.3968	10	0.076	15	2.30	11.89
	3120.359	2.43	6.41	4	6	1.46	0.3199	10	0.075	15	3.67	19.25
	3124.973	2.45	6.42	6	8	1.65	0.3223	8	0.074	15	5.47	29.06
	3128.692	2.43	6.40	4	4	0.505	0.0742	11	0.071	15	0.86	4.74
	3132.053	2.48	6.44	8	10	1.86	0.3421	7	0.072	15	7.60	41.48
	3136.681	2.45	6.41	6	6	0.436	0.0643	11	0.073	0	1.10	5.92
	3147.220	2.48	6.42	8	8	0.25	0.0371	9	0.073	0	0.83	4.48

[a]The lines at 2677.159 Å and 2677.161 Å have been grouped, and the resulting data are indicated
[b]Data from Ref. [49].
[c]Data from Ref. [50].
[d]Calculated for T = 14000 K.
[e]Calculated for T = 14000 K, N_e = 2.5x10^{17} cm^{-3}.

Figures

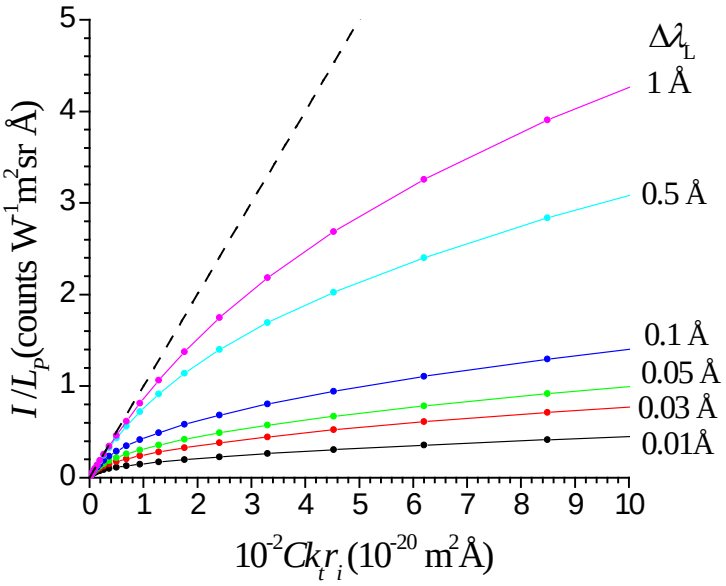

Fig. 1. Line intensity, normalized to the Planck radiance, calculated as a function of $10^{-2} C\, k_t r_i$ for different values of the Lorentzian width $\Delta\lambda_L$ and a common Doppler width $\Delta\lambda_D$ =0.03 Å. The dashed line is the common linear limit of the curves.

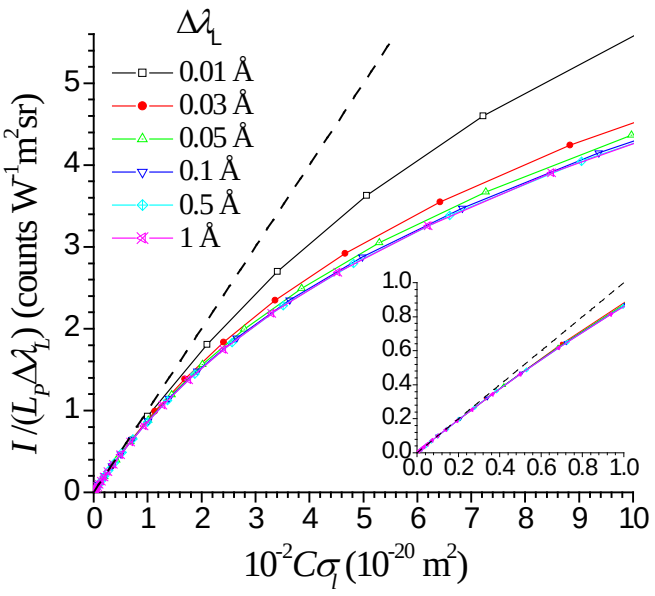

Fig. 2. Line intensity, normalized to the Planck radiance and the Lorentzian width $\Delta\lambda_L$, calculated as a function of $10^{-2}C\sigma_l$ for different values of the Lorentzian width and a common Doppler width $\Delta\lambda_D$ =0.03 Å. The dashed line is the common linear limit of the curves.

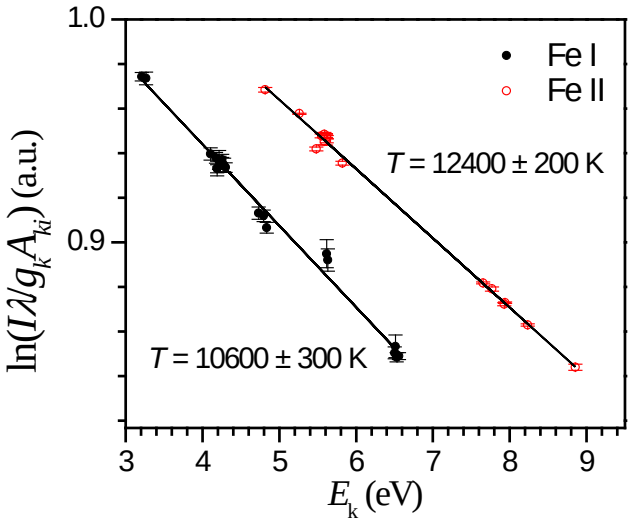

Fig. 3. Boltzmann plots for Fe II and Fe I lines measured with a time delay of 2.6 μs and a width of 0.8 μs. The apparent temperatures deduced from the fittings to straight lines are indicated.

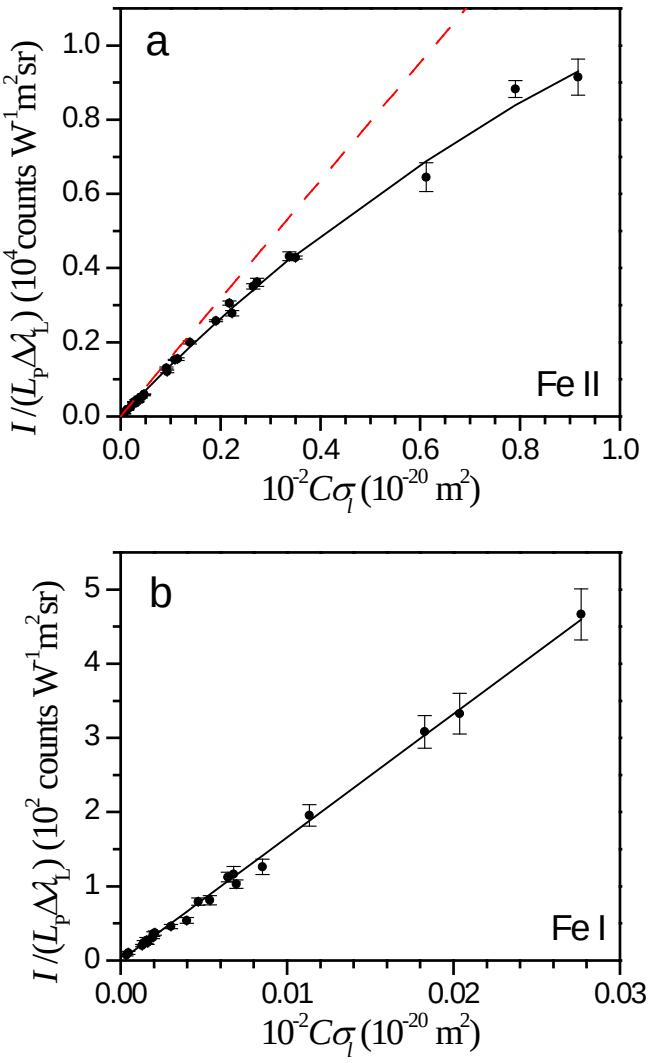

Fig. 4. $C\sigma$ graphs for Fe II (a) and Fe I (b) lines measured with a time delay of 2.6 μs and a width of 0.8 μs. The solid lines are the fittings to $C\sigma$ curves and the dashed line in (a) is the linear limit of the curve for $C\sigma_l \to 0$.

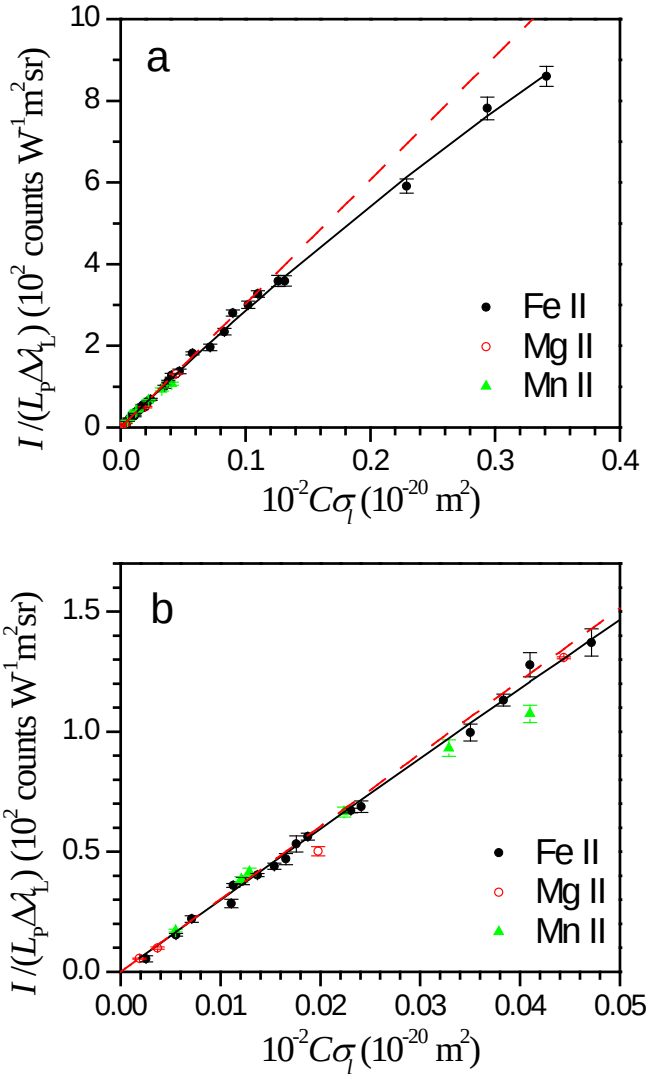

Fig. 5. (a) $C\sigma$ graph for Fe II, Mn II and Mg II lines measured with a time delay of 1.15 μs and a width of 0.3 μs. The solid line is the fitting to a $C\sigma$ curve and the dashed line is the linear limit of the curve for $C\sigma_l \to 0$. (b) The same plot for low values of $10^{-2}C\sigma_l$.

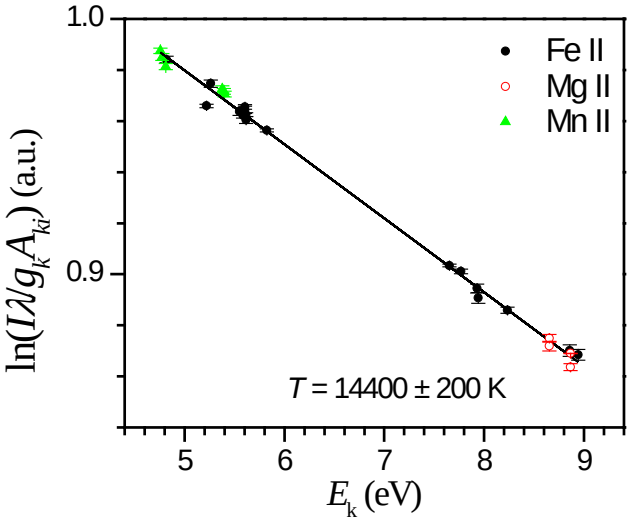

Fig. 6. Multi-element Boltzmann plot for Fe II, Mn II and Mg II lines measured with a time delay of 1.15 μs and a width of 0.3 μs. The apparent temperature deduced from the fitting to a straight line is indicated.

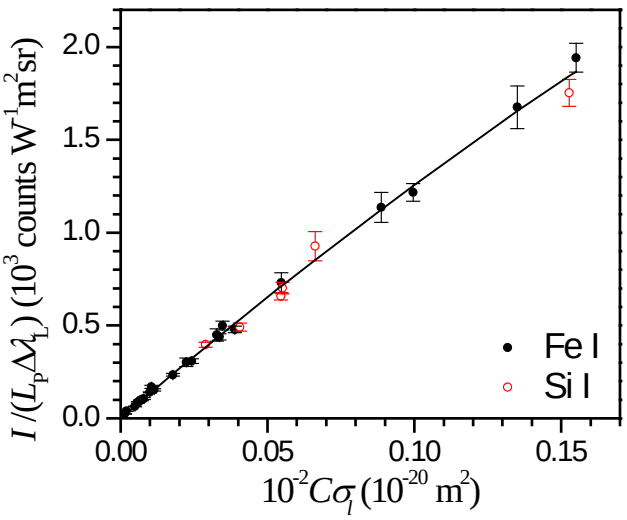

Fig. 7. (a) $C\sigma$ graph for Fe I, and Si I lines measured with a time delay of 3 μs and a width of 1 μs. The solid line is the fitting to a $C\sigma$ curve.

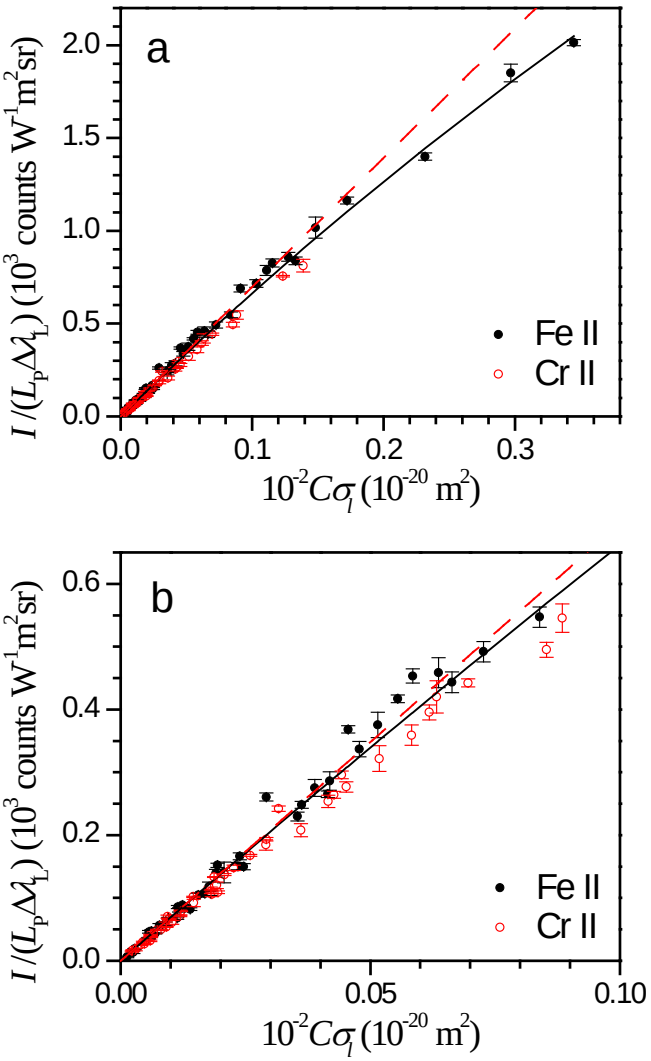

Fig. 8. (a) $C\sigma$ graph for Fe II and Cr II lines measured with a time delay of 1.15 μs and a width of 0.3 μs using two samples with different concentrations of Fe and Cr. The solid line is the fitting to a $C\sigma$ curve and the dashed line is the linear limit of the curve for $C\sigma_l \to 0$. (b) The same plot for low values of $10^{-2}C\sigma_l$